

Velocity-Based Cardiac Contractility Personalization from Images using Derivative-Free Optimization

Journal:	<i>Transactions on Medical Imaging</i>
Manuscript ID:	TMI-2014-0106
Manuscript Type:	Full Paper
Date Submitted by the Author:	03-Feb-2014
Complete List of Authors:	Wong, Ken C. L.; National Institutes of Health, Clinical Center Sermesant, Maxime; Inria, Asclepios Rhode, Kawal; King's College London, Division of Imaging Sciences Ginks, Matthew; King's College London, Interdisciplinary Medical Imaging Group Rinaldi, C. Aldo; Guy's and St Thomas' Hospital Trust, Cardiology Razavi, Reza; Kings College London, Division of Imaging Sciences Delingette, Hervé; INRIA , ASCLEPIOS Ayache, Nicholas; INRIA, Asclepios
Keywords:	Optimization < General methodology, Biomechanical modeling < General methodology, Finite element modeling < General methodology, Quantification and estimation < General methodology, Heart < Object of interest, Magnetic resonance imaging (MRI) < Imaging modalities
Specialty/Area of Expertise:	Cardiac contractility, Cardiac electromechanical model, Derivative-free optimization, Model personalization, Parameter estimation

Velocity-Based Cardiac Contractility Personalization from Images using Derivative-Free Optimization

Ken C. L. Wong, Maxime Sermesant, Kawal Rhode, Matthew Ginks, C. Aldo Rinaldi, Reza Razavi, Hervé Delingette, and Nicholas Ayache

Abstract—Model personalization is a key aspect for biophysical models to impact clinical practice, and cardiac contractility personalization from medical images is a major step in this direction. Existing gradient-based optimization approaches show promising results of identifying the maximum contractility from images, but the contraction and relaxation rates are not accounted for. A main reason is the limited choices of objective functions when their gradients are required. For complicated cardiac models, analytical evaluations of gradients are very difficult if not impossible, and finite difference approximations are computationally expensive and may introduce numerical difficulties. By removing such limitations with derivative-free optimization, we found that a velocity-based objective function can properly identify the maximum contraction, contraction rate, and relaxation rate simultaneously with intact model complexity. Experiments on synthetic data show that the parameters are better identified using the velocity-based objective function than its position-based counterpart. Experiments on clinical data show that the framework can obtain personalized contractility consistent with the physiologies of patients and healthy volunteers.

Index Terms—Cardiac contractility, cardiac electromechanical model, derivative-free optimization, model personalization, parameter estimation.

I. INTRODUCTION

Cardiac model personalization is a process to obtain a biophysical model accounting for the subject-specific cardiac physiology, usually realized as parameter estimation. Given a generic cardiac model designed from invasive experiments of anatomy, electrophysiology, and cardiac mechanics, the corresponding model parameters are estimated from the subject-specific *in vivo* measurements such as non-contact endocardial mappings and magnetic resonance images (MRI). As simulation of the whole organ has reached a degree of realism which is quantitatively comparable with available cardiac images and signals acquired routinely on patients, model personalization gives a potential impact to clinical practice by improving disease diagnoses and planning therapies such as cardiac resynchronization therapy [1].

Cardiac mechanics is the interaction among active contraction stresses, passive mechanical properties (stiffness), and boundary conditions exerted by surrounding anatomical structures [2], [3]. Various cardiac electromechanical models have been proposed to describe such an interaction with different physiological plausibilities, complexities, and computational efficiencies [4], [5], [6], [7]. According to the characteristics of the models, different personalization algorithms have been proposed. In [8], the homogeneous and transversely isotropic Young's moduli of a piece-wise linear passive mechanical

model were estimated with the active contraction using an expectation-maximization (EM) algorithm from tagged MRI. In [9], the heterogeneous and isotropic Young's moduli and Poisson's ratios were estimated simultaneously with cardiac deformation using an extended Kalman filter-based EM algorithm from cine and tagged MRI. In [10], the regional maximum contractions were estimated using reduced unscented Kalman filtering (rUKF) from porcine cine MRI. In [11], homogeneous passive material stiffness of a nonlinear transversely isotropic model was estimated with a sequential quadratic programming (SQP) method from tagged MRI and *ex vivo* DT-MRI of canine hearts. In [12], the performances of rUKF and SQP for the estimation of stiffness parameters were compared on synthetic data. In [13], a method based on the unscented transform algorithm was proposed to calibrate the global mechanical parameters of the Bestel-Clément-Sorine electromechanical model to aid model personalization.

In this paper, the concentration will be on cardiac contractility personalization. In our previous work [14], the gradient-based quasi-Newton L-BFGS-B algorithm was utilized to optimize a position-based objective function. Although the utilized adjoint method allows efficient computation of the gradient, it requires the system derivatives of the complicated cardiac electromechanical model. This limits the exploration of the proper objective functions and also the types of parameters to be estimated, as some objective functions are highly nonlinear with respect to the desired parameters. Therefore, only the maximum contraction was estimated in [14] even after some model simplifications.

In consequence, we propose the use of derivative-free optimization for cardiac contractility personalization. Without the analytical, numerical, and computational difficulties associated with gradient evaluation, objective functions which may provide better parameter estimation can be investigated with relative ease. By using derivative-free optimization, we propose a velocity-based objective function for simultaneous estimation of regional maximum contraction, rate of contraction, and rate of relaxation. Experiments were performed on synthetic data to show the capability of the framework in identifying regional contractility, and its sensitivity to noise and initial parameters. Experiments on patient and volunteer data also show its clinical relevance.

II. CARDIAC ELECTROMECHANICAL MODEL

In the computational environment, the personalized cardiac geometry can be represented as points bounded by surfaces.

Using numerical methods such as finite element methods (FEM) [15], [6] or meshfree methods [16], [7], the dynamics of a cardiac electromechanical model can be given as:

$$\mathbf{M}\ddot{\mathbf{U}} + \mathbf{C}\dot{\mathbf{U}} + \mathbf{K}\mathbf{U} = \mathbf{F}_b + \mathbf{F}_c \quad (1)$$

where \mathbf{M} , \mathbf{C} , and \mathbf{K} are the mass, damping, and stiffness matrices, and $\ddot{\mathbf{U}}$, $\dot{\mathbf{U}}$, and \mathbf{U} are the acceleration, velocity, and displacement vectors. \mathbf{F}_b comprises the boundary conditions of simulated blood pressures and displacement constraints. \mathbf{F}_c is the active contraction force vector derived from electrophysiology and tissue structure. The electromechanical model in [6] is used in this paper.

To obtain \mathbf{F}_c , the relation between the action potential and the active contraction can be modeled as [6]:

$$\frac{\partial\sigma_c}{\partial t} + \sigma_c = u\sigma_0 \quad (2)$$

with σ_c the contraction stress, u the normalized action potential, and σ_0 is the maximum contraction parameter defining the maximum value of σ_c . As u is between 0 and 1 and the changes of depolarization and repolarization are abrupt, the solution of (2) can be approximated as:

$$\begin{cases} \sigma_c(t) = \sigma_0(1 - e^{\alpha_c(T_d-t)}) & \text{if } T_d \leq t \leq T_r \\ \sigma_c(t) = \sigma_c(T_r)e^{\alpha_r(T_r-t)} & \text{if } T_r < t < T_d + HP \end{cases} \quad (3)$$

where HP is the heart period. α_c and α_r are the contraction and relaxation rates added to better control the change of σ_c . T_d and T_r are the depolarization and repolarization times derived from the action potential, and a time constant can be added to model the delay between the electrical and mechanical phenomena. Therefore, the parameters of interest are σ_0 , α_c , and α_r . Although this model is relatively simple, it is capable of simulating realistic cardiac cycles [17], and its simplicity facilitates the complicated parameter estimation. With \mathbf{F}_c providing the active contraction, \mathbf{F}_b providing the boundary conditions, and \mathbf{M} , \mathbf{C} , \mathbf{K} providing the passive mechanical properties, the cardiac cycle can be simulated.

III. ELECTROPHYSIOLOGY AND KINEMATICS PERSONALIZATION

A. Electrophysiology Personalization

To avoid accumulating sources of uncertainties, patient-specific datasets including a rich description of cardiac electrophysiology were utilized. In addition to the acquisition of anatomical and cine MRI, non-contact endocardial mappings have been acquired at King's College London, St Thomas' Hospital during electrophysiology studies in an XMR suite [18], both in sinus rhythm and during specific stimulation protocols. The extracted depolarization and repolarization isochrones then serve as input information to an electrophysiology personalization method [19] which minimizes the discrepancy between measured and simulated isochrones. Its output is a set of global parameters and local parameters (electrical conductivities) of the Mitchell-Schaeffer electrophysiology model which allow to interpolate, extrapolate and regularize the acquired isochrones. The personalized depolarization and repolarization times are then used to control the active contraction force of the mechanical model described in the next section.

B. Kinematics Personalization

Kinematics personalization consists in estimating the motion of cardiac structures from images. The same electromechanical model is used for both the regularization of the cardiac motion from cine MRI and the estimation of the biophysical parameters. This leads to a velocity field which is consistent with the one produced by the electromechanical model during the mechanical parameter estimation, in terms of smoothness and spatial resolution. The kinematics personalization approach in [20] is used with the cardiac electromechanical model in Section II. The two ventricles are meshed with tetrahedra from the anatomical MRI (Fig. 1). The evolution of the displacement of each mesh node is governed by (1) with an embedded image force:

$$\mathbf{M}\ddot{\mathbf{U}} + \mathbf{C}\dot{\mathbf{U}} + \mathbf{K}\mathbf{U} = \mathbf{F}_b + \mathbf{F}_c + \beta\mathbf{F}_{\text{img}} \quad (4)$$

In the kinematics personalization, \mathbf{F}_{img} corresponds to a force vector which tracks salient image features in the image sequence, computed using a 3D block-matching algorithm to attract points towards the nearest edge voxels. To balance between model regularization and data attachment, we set β based on a sensitivity analysis [21], so that the personalized cardiac deformation is smooth while consistent with the apparent motion from the images. Image forces are not physiology based since their sole purpose is to help tracking the cardiac motion, and they are discarded during the mechanical personalization. The personalized nodal positions and velocities are obtained from the kinematics personalization, which are used as the inputs for contractility personalization, along with the personalized electrophysiology.

IV. MECHANICS PERSONALIZATION WITH DERIVATIVE-FREE OPTIMIZATION

Kinematics personalization produces cardiac motion consistent with the apparent motion in the images. Nevertheless, it cannot address the underlying physiological properties of the patient, such as the active contraction properties. To infer the physiological properties, mechanics personalization is required. Although a more complete mechanics personalization should address both active and passive parameters, here we only concentrate on the active parameters to reduce the complexity of the problem. To perform contractility personalization through variational data assimilation, an objective function and an optimization algorithm are required.

A. Objective Function

1) *Formulation:* The similarity between simulations and measurements is defined by an objective function. Supposing that the heart geometry is partitioned into regions, the objective function for variational data assimilation can be given as:

$$\mathcal{F}(\boldsymbol{\theta}) = \sum_k w_k \sum_r w_r \left(\frac{\sum_i \|\bar{\mathbf{y}}_{k,i} - \mathbf{y}_{k,i}(\boldsymbol{\theta})\|^2}{n_r} \right) \quad (5)$$

where $\boldsymbol{\theta}$ is a vector comprising parameters (σ_0 , α_c , α_r) of all regions. $\bar{\mathbf{y}}_{k,i}$ is the measurement at discrete time instant k of point i in region r , and $\mathbf{y}_{k,i}(\boldsymbol{\theta})$ is the corresponding simulated

1 quantity. n_r is the number of measurements in a region, and w_k
 2 and w_r are the weights of different time instants and regions.
 3

4 The measurements $\bar{\mathbf{y}}_{k,r}$ are extracted from patient data,
 5 which are the personalized kinematic quantities in our case.
 6 Therefore, a time instant k does not necessarily correspond
 7 to an image frame, but a time frame in the kinematics
 8 personalization. n_r is used to remove the bias towards regions
 9 with more measurements, but can be omitted if bias is desired.
 10 The weights w_k and w_r can be used to emphasize different
 11 time instants or regions. For example, if the contraction phase
 12 is of more interest, w_k can be larger for the corresponding
 13 time instants. Similarly, regions with better measurements can
 14 have larger w_r . Nevertheless, as the optimal weights have not
 15 been studied and are dependent on applications and situations,
 16 they were set to 1 in the experiments.

17 Different types of measurements $\bar{\mathbf{y}}_{k,r}$ can give different
 18 results. In [17], [22], [14], the positions of the personalized
 19 cardiac kinematics were used. As only the maximum con-
 20 traction parameters σ_0 were estimated, the use of measured
 21 positions can provide meaningful results. Nevertheless, if the
 22 rates α_c and α_r are also desired, positions alone may not
 23 provide the necessary temporal information. Furthermore, it
 24 has been shown using control theory that velocity-based data
 25 assimilation can lead to a stable system [23]. Therefore, we
 26 propose to use velocities instead.

27 To show the difference between using positions and veloci-
 28 ties in (5), let $\Delta\mathbf{u}_{k,i}$ be the incremental displacement at time
 29 instant k of point i with time step Δt_k , where Δt_k is the time
 30 step of numerical time integration when solving (1). Therefore,
 31 at time instant \tilde{k} , the velocity is $\mathbf{v}_{\tilde{k},i} = \Delta\mathbf{u}_{\tilde{k},i}/\Delta t_{\tilde{k}}$, and the
 32 position is $\mathbf{x}_{\tilde{k},i} = \mathbf{x}_{0,i} + \sum_{k=1}^{\tilde{k}} \Delta\mathbf{u}_{k,i}$. Assuming the same
 33 time steps and initial positions are used by both personalized
 34 kinematics and simulation, the position difference gives:

$$\bar{\mathbf{y}}_{\tilde{k},i} - \mathbf{y}_{\tilde{k},i} = \bar{\mathbf{x}}_{\tilde{k},i} - \mathbf{x}_{\tilde{k},i} = \sum_{k=1}^{\tilde{k}} \Delta\bar{\mathbf{u}}_{k,i} - \Delta\mathbf{u}_{k,i} \quad (6)$$

35 which is actually the sum of incremental displacement dif-
 36 ferences of all previous time steps. Therefore, the temporal
 37 information cannot be properly reflected. On the other hand,
 38 the velocity difference gives:

$$\bar{\mathbf{y}}_{\tilde{k},i} - \mathbf{y}_{\tilde{k},i} = \bar{\mathbf{v}}_{\tilde{k},i} - \mathbf{v}_{\tilde{k},i} = \frac{\Delta\bar{\mathbf{u}}_{\tilde{k},i} - \Delta\mathbf{u}_{\tilde{k},i}}{\Delta t_{\tilde{k}}} \quad (7)$$

39 thus the temporal information is better preserved. In conse-
 40 quence, velocities are preferable when α_c and α_r are desired.

41 2) *Landscape Investigation*: To further analyze the dif-
 42 ference between position-based and velocity-based objective
 43 functions, a one-region case was investigated (Fig. 2). Cardiac
 44 cycles were simulated on a patient heart geometry (see Section
 45 V-A) with identical setting but different values of σ_0 , α_c , and
 46 α_r . The heart geometry was treated as one region, and a total
 47 of 448 simulations were performed (σ_0 : 60-120 kPa with stride
 48 = 10 kPa; α_c and α_r : 5-40 s⁻¹ with stride = 5 s⁻¹). By
 49 using one of the simulations as the reference ($\sigma_0 = 90$ kPa,
 50 $\alpha_c = \alpha_r = 25$ s⁻¹), the 3D objective functions were computed.
 51 To visualize the 2D landscapes, the cutting planes centering
 52 at the reference parameters are shown.

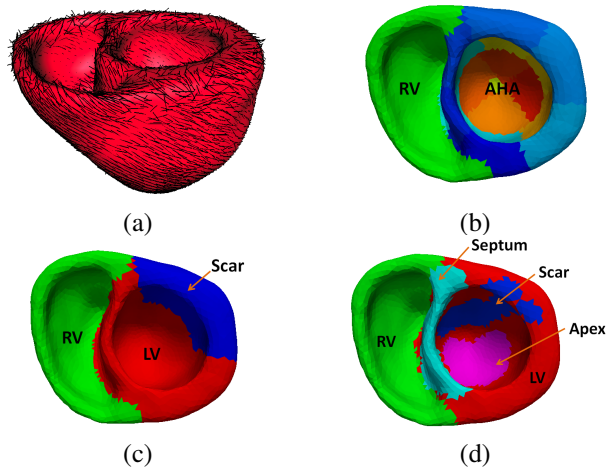


Fig. 1. Heart representation. (a) Heart geometry and fiber orientations. (b) AHA-zone representation. (c) 3-zone representation. (d) 5-zone representation.

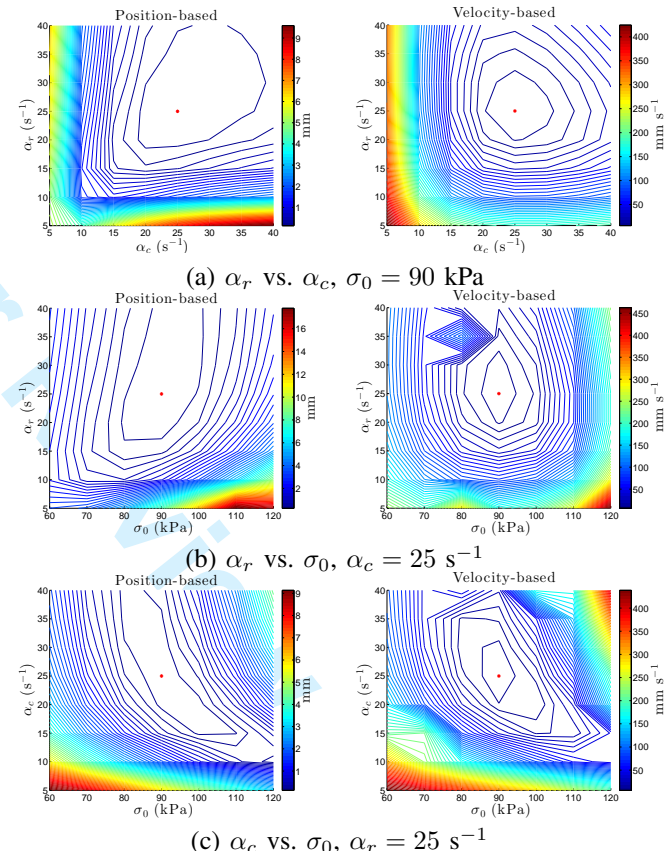


Fig. 2. Landscapes of position-based and velocity-based objective functions, computed from simulated cardiac cycles. The red * indicates the reference parameters ($\sigma_0 = 90$ kPa, $\alpha_c = \alpha_r = 25$ s⁻¹).

Fig. 2 shows that the velocity-based objective function has better landscapes than the position-based one. The position-based landscapes have relatively flat valleys, thus the minimum is more difficult to be identified as the values around are similar. Fig. 2(a) shows that the velocity-based objective function is more capable of identifying contraction and relaxation rates. Fig. 2(b) and (c) show that both objective functions have similar capability of identifying maximum contraction, as they

have similar changes in the σ_0 direction. Nevertheless, the position-based objective function is less capable of identifying the rate parameters as there are long valleys in the α_c and α_r directions. These observations are consistent with the explanations in the previous section that the rate information is better preserved with the velocity-based objective function.

B. Derivative-Free Optimization

To estimate the contraction parameters, the optimization problems were solved using gradient-based algorithms on synthetic data in [17], [22], and on clinical data in [14]. In [14], the gradient-based quasi-Newton L-BFGS-B algorithm was used. Although the adjoint method was used for efficient gradient computation, the required derivatives of the electromechanical model are difficult to derive analytically as the model involves interactions between myocardial deformation, ventricular pressures, contraction stresses, and different boundary conditions. Therefore, it is hard to compute the gradient analytically without making significant simplifications which sacrifice the model integrity and thus the estimation accuracy. In consequence, analytical gradient evaluation may limit the flexibility of choosing the appropriate objective function, and the accuracy and stability may be reduced if improper simplifications are made [24].

On the other hand, although finite difference is a popular numerical alternative when analytical evaluation of the gradient is infeasible [25], the associated computational complexity is impractical to our problem. Let n be the number of parameters to be estimated. $n + 1$ function evaluations are required for the forward or backward approximations, and $2n + 1$ function evaluations are required for the more accurate central difference approximation. As each function evaluation involves the simulation of the whole cardiac cycle, finite difference is impractical. Furthermore, finite difference is sensitive to the sampling distance and noise of the objective function [25]. Therefore, it is not the optimal choice to our problem.

Some optimization methods assume that the objective function is locally quadratic, such as the BFGS and the BOBYQA algorithms [26]. These methods can be fast and accurate when the locally quadratic assumption is satisfied. Nevertheless, as the objective functions of our problem are non-quadratic (Fig. 2), the use of these methods may lead to suboptimal results.

With respect to these issues, direct search methods which make few assumptions about the objective function are more preferable, and the subplex method (SUBPLEX) is adopted [27]. SUBPLEX is a generalization of the Nelder-Mead simplex method (NMS) [28]. A simplex in n -dimensional space is a convex hull of $n + 1$ points, for example, a triangle in 2D and a tetrahedron in 3D. In the NMS method, a simplex moves through the objective function space, changing size and shape, and shrinking near the minimum. The NMS method performs well when the dimension is small (e.g. ≤ 5), but can be inefficient when the dimension is much higher [27]. To address this issue, SUBPLEX decomposes the high-dimensional space into subspaces that the NMS method can search efficiently. Therefore, SUBPLEX inherits the ability of handling noisy objective functions but more computationally efficient.

TABLE I
YOUNG'S MODULI (E_f , E_{cf}) AND POISSON'S RATIOS (ν_f , ν_{cf}) ALONG AND ACROSS FIBER. ADOPTED FROM [2].

E_f	E_{cf}	ν_f	ν_{cf}
75 kPa	25 kPa	0.47	0.47

TABLE II
SYNTHETIC DATA. GROUND-TRUTH PARAMETERS.

3-zone	LV	RV	Scar
σ_0 (kPa)	100	80	50
α_c (s^{-1})	30	25	10
α_r (s^{-1})	25	20	5

5-zone	LV	RV	Scar	Septum	Apex
σ_0 (kPa)	100	60	40	80	80
α_c (s^{-1})	30	20	15	25	25
α_r (s^{-1})	25	15	10	20	20

V. EVALUATION ON SYNTHETIC DATA

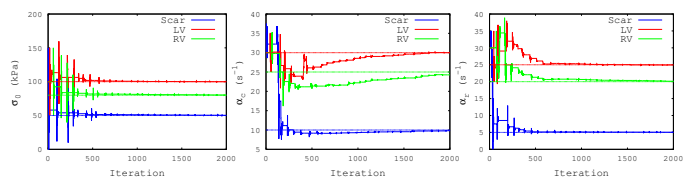
To evaluate the performance of our framework, experiments were performed on synthetic data. Comparisons between the position-based and velocity-based object functions, and also the sensitivity of the velocity-based framework with respect to measurement noise and initial parameters, are presented.

A. Experimental Setups

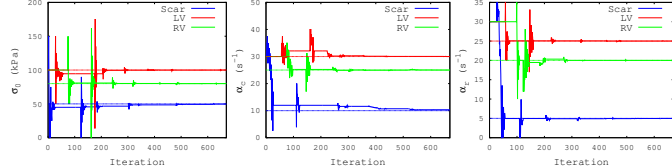
The heart representation was created from the data of a patient with myocardial infarction. The heart geometry was segmented from the image frame at mid-diastole, and a FEM mesh with synthetic fiber orientations was obtained (Fig. 1(a)). The personalized T_d and T_r derived from the patient noncontact endocardial electrical mappings were used in (3) [19]. The passive mechanical parameters used are shown in Table I. To show that our framework can be used with different types of zone partitioning, three settings were tested:

- 1) AHA-zone representation (Fig. 1(b)): the American Heart Association (AHA) nomenclature [29] was used for the left ventricle. The right ventricle is one zone (RV).
- 2) 3-zone representation (Fig. 1(c)): AHA zones 4, 5, 10, and 11 were grouped into one zone (Scar), and the remaining AHA zones were grouped into another zone (LV). The right ventricle is one zone (RV).
- 3) 5-zone representation (Fig. 1(d)): the infarcted region was identified from late-enhanced MRI (Scar). The rest of the left ventricle was partitioned into LV, Septum, and Apex. The right ventricle is one zone (RV).

Two simulations with active contraction parameters listed in Table. II were performed on the 3-zone and 5-zone representations to provide the ground truth measurements. To emulate the condition of using real data, only the positions and velocities on the heart surfaces were used for the parameter estimations. The AHA-zone representation was only used for the parameter estimation with the 3-zone measurements to verify if the framework is capable of estimating high-dimensional parameters. The initial parameters were $\sigma_0 = 100$ kPa, $\alpha_c = \alpha_r = 30 s^{-1}$, which were used in all experiments in this paper (except the initial parameter tests). The lower

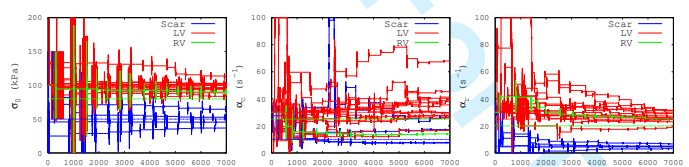


(a) Position-based optimization.

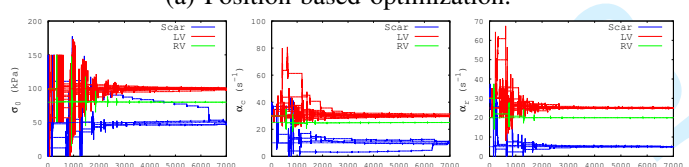


(b) Velocity-based optimization.

Fig. 3. Synthetic data. Estimation of 3-zone parameters, with dotted lines representing the ground truth values. Left to right: maximum contraction parameter σ_0 , contraction rate α_c , and relaxation rate α_r .



(a) Position-based optimization.



(b) Velocity-based optimization.

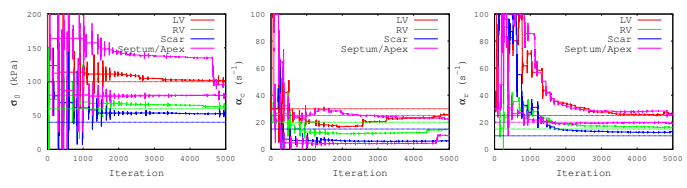
Fig. 4. Synthetic data. Estimation of AHA-zone parameters, with dotted lines representing the ground truth values. Left to right: maximum contraction parameter σ_0 , contraction rate α_c , and relaxation rate α_r .

and upper bounds of σ_0 are 0 kPa and 200 kPa, and the lower and upper bounds of α_c and α_r are 0 s^{-1} and 100 s^{-1} . As the objective functions are relatively flat around the optimal points, to avoid immature convergence, small absolute parameter tolerances were used as the convergence criteria, with $\sigma_0 = 0.5$ kPa, $\alpha_c = \alpha_r = 0.05$ s^{-1} . The maximum numbers of iterations of the 3-zone, 5-zone, and AHA-zone estimations were 2000, 5000, and 7000 respectively, which were chosen empirically.

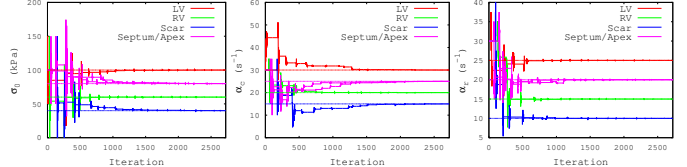
B. Results

Fig. 3 shows the estimations of 3-zone parameters, and both position-based and velocity-based optimizations have good results. Nevertheless, the velocity-based optimization converged after 670 iterations, while the position-based optimization did not converge with the maximum number of iterations (2000).

To verify the capability of estimating high-dimensional parameters, estimations were performed using the AHA-zone representation with the 3-zone measurements (Fig. 4). Although both optimizations did not converge with the maximum number of iterations (7000) because of the restrictive convergence criteria, the velocity-based optimization obtained

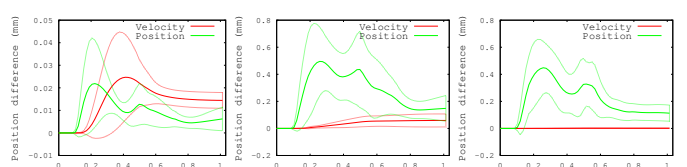


(a) Position-based optimization.



(b) Velocity-based optimization.

Fig. 5. Synthetic data. Estimation of 5-zone parameters, with dotted lines representing the ground truth values. Left to right: maximum contraction parameter σ_0 , contraction rate α_c , and relaxation rate α_r .



(a) 3-zone. (b) AHA-zone. (c) 5-zone.

Fig. 6. Synthetic data. Mean position differences of all nodes between the ground truth and the personalized simulations in a cardiac cycle. The dotted lines envelop the standard deviation.

much better results. This is consistent with the observation in Fig. 2 that the position-based objective function has a larger flat region, which effect is amplified in the high-dimensional parameter estimation.

To show that the framework can be applied to different types of zone partitioning, experiments were performed on the 5-zone representation (Fig. 5). Similar to the AHA-zone estimation, the velocity-based optimization has much better results, and converged after 2724 iterations. On the other hand, the position-based optimization did not converge within the maximum number of iterations (5000).

Fig. 6 shows the mean position differences between the ground truth and the personalized simulations of all nodes in a cardiac cycle. For the 3-zone optimization, the mean position differences of both position-based and velocity-based optimizations are too small (< 0.05 mm) to be meaningfully compared. For the AHA-zone and 5-zone optimizations, the velocity-based optimizations are much better. Especially for the 5-zone optimization, the standard deviation of the velocity-based estimation is too small to be visualized when put together with the position-based optimization.

To verify the sensitivity of the framework with respect to measurement noise, the 3-zone measurements were added with zero-mean noises of different signal-to-noise ratios (SNR = 1, 2, and 5), and the velocity-based optimizations were performed. Fig. 7 shows that the estimated parameters are almost identical to the ground truth, even in the worst case when the SNR = 1. One reason of such robustness is the use of variational data assimilation. In fact, even with the noisy

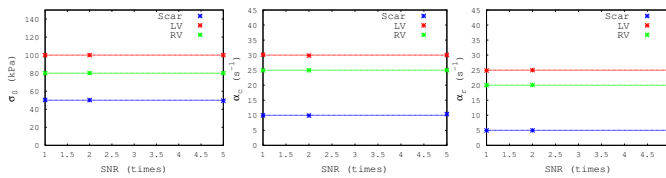


Fig. 7. Synthetic data. Estimated 3-zone parameters with different SNR. The * indicate the estimated parameters, and the dotted lines represent the ground truth values. Left to right: maximum contraction parameter σ_0 , contraction rate α_c , and relaxation rate α_r .

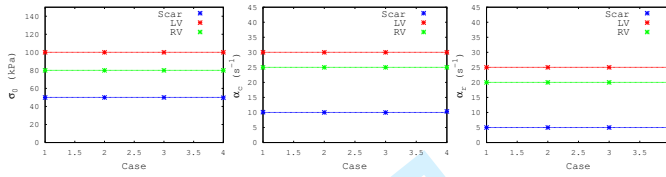


Fig. 8. Synthetic data. Estimated 3-zone parameters with different initializations (Case 1: $\sigma_0 = 50$ kPa, $\alpha_c = \alpha_r = 5$ s $^{-1}$; Case 2: $\sigma_0 = 50$ kPa, $\alpha_c = \alpha_r = 30$ s $^{-1}$; Case 3: $\sigma_0 = 100$ kPa, $\alpha_c = \alpha_r = 5$ s $^{-1}$; Case 4: $\sigma_0 = 100$ kPa, $\alpha_c = \alpha_r = 30$ s $^{-1}$). The * indicate the estimated parameters, and the dotted lines represent the ground truth values. Left to right: maximum contraction parameter σ_0 , contraction rate α_c , and relaxation rate α_r .

measurements, the objective function (5) is still smooth as the measurements are the same at any θ . Therefore, as long as the noises are zero-mean, their effects to the estimation should be minimal. This can be shown by the similar numbers of iterations (654, 649, and 665, for SNR = 1, 2, and 5).

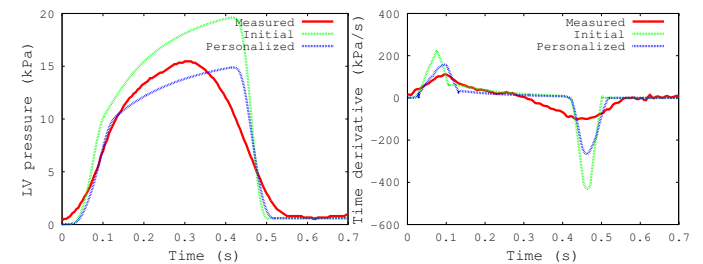
To verify the sensitivity of the framework with respect to different initial parameters, 3-zone velocity-based optimizations were performed with different initializations (Case 1: $\sigma_0 = 50$ kPa, $\alpha_c = \alpha_r = 5$ s $^{-1}$; Case 2: $\sigma_0 = 50$ kPa, $\alpha_c = \alpha_r = 30$ s $^{-1}$; Case 3: $\sigma_0 = 100$ kPa, $\alpha_c = \alpha_r = 5$ s $^{-1}$; Case 4: $\sigma_0 = 100$ kPa, $\alpha_c = \alpha_r = 30$ s $^{-1}$). Fig. 8 shows that the framework is robust to initializations, which means that the suplex algorithm matches the characteristics of the objective function. The number of iterations from Case 1 to 4 are 729, 694, 980, and 670 respectively.

VI. EVALUATION ON CLINICAL DATA

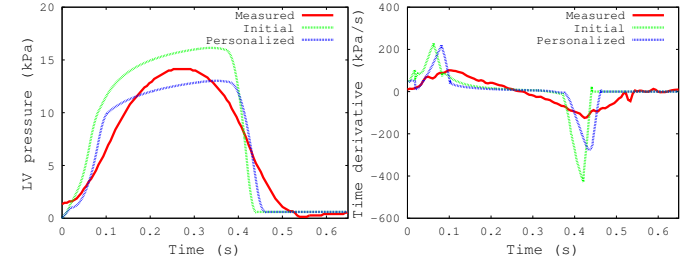
To verify the clinical applicability of the proposed framework, experiments were performed on clinical data from patients and healthy volunteers. These experiments are to validate, in terms of the consistency with the personalized kinematics, if the personalization framework can provide parameters reflecting the actual physiology of the subject.

A. Patients with Cardiac Diseases

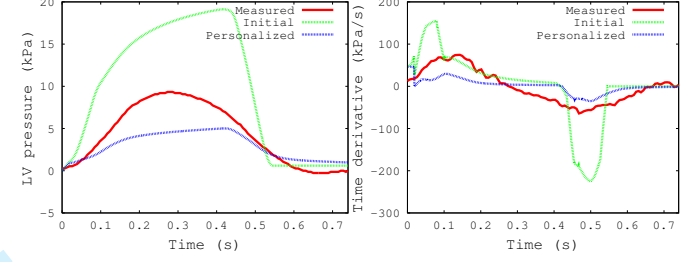
1) Experimental Setups: Three data sets have been tested. Patient 1 has myocardial infarction, whose data set was used in Section V-A to generate the synthetic data, with the infarcted regions identified through late-enhanced MRI. Patient 2 and 3 have dilated cardiomyopathy but without identified infarctions. All patients have left bundle branch block (LBBB) and suffer from heart failure. The numbers of frames of Patient 1, 2, and 3 are 30 (1.03 s), 30 (0.73 s), and 40 (1.07 s) respectively. The corresponding in-plane resolutions are 1.56, 1.45,



(a) Patient 1.



(b) Patient 2.



(c) Patient 3.

Fig. 9. Patient data. Results of velocity-based optimization. Left: LV pressures. Right: the corresponding time derivatives.

and 1.52 mm 2 , and all images have inter-slice resolution of 10 mm. All data sets have the endocardial activation maps measured with the Ensite balloon (St. Jude Medical, MN), which were extrapolated to the myocardial volume using an electrophysiological model to provide the subject-specific T_d and T_r in (3) for the experiments [19].

For each data set, the heart geometry was segmented from the image frame at mid-diastole, and a FEM mesh with synthetic fiber orientations was constructed [1]. For Patient 1, the 5-zone heart representation in Section V-A was used (Fig. 1 (d)) with the known scar region. For Patient 2 and 3, AHA-zone representations similar to that in Fig. 1 (b) were used. Only the points on the heart surfaces were used as motion information is unavailable inside the myocardium for cine MRI. The performance and noise-handling capability of the kinematics personalization have been studied in [30], [20], [21]. The same passive mechanical parameters, initial parameters, lower and upper bounds, and convergence criteria in Section V-A were applied. The maximum number of iterations was 5000.

2) Results: Table III shows the estimated parameters from the position-based and velocity-based optimization. For Patient 1 (5-zone representation), the maximum contractions (σ_0) are similar, both with higher values at the LV and RV, but lower values at the scar, septum, and apex. On the other hand, the

TABLE III
PATIENT DATA. ESTIMATED CONTRACTION PARAMETERS.

Patient 1 (position-based)							Patient 1 (velocity-based)						
Zone	LV	RV	Scar	Septum	Apex		Zone	LV	RV	Scar	Septum	Apex	
σ_0 (kPa)	80.0	81.7	56.4	62.5	57.3		σ_0 (kPa)	83.9	81.9	50.6	54.4	47.2	
α_c (s^{-1})	19.5	11.7	15.3	5.4	11.9		α_c (s^{-1})	30.1	13.9	34.1	42.4	30.4	
α_r (s^{-1})	100.0	92.6	16.0	7.1	8.3		α_r (s^{-1})	35.9	28.2	53.6	6.9	47.6	

Patient 2 (position-based)																		
Zone	1	2	3	4	5	6	7	8	9	10	11	12	13	14	15	16	17	RV
σ_0 (kPa)	72.3	61.0	64.1	67.3	71.5	79.2	113.4	200.0	82.0	93.4	56.9	70.4	41.5	50.7	59.6	54.5	200.0	83.6
α_c (s^{-1})	5.1	4.4	3.7	15.8	28.4	16.3	5.6	25.3	5.0	11.2	21.4	21.4	9.8	9.1	7.9	5.3	100.0	9.5
α_r (s^{-1})	33.3	39.7	100	25.1	100.0	100.0	100.0	100.0	95.1	99.7	28.2	6.8	10.2	13.4	25.4	9.6	21.5	

Patient 2 (velocity-based)																		
Zone	1	2	3	4	5	6	7	8	9	10	11	12	13	14	15	16	17	RV
σ_0 (kPa)	59.3	68.2	33.8	70.8	64.6	81.7	93.3	174.7	135.4	76.9	68.3	62.6	34.2	52.0	44.6	37.4	184.5	71.3
α_c (s^{-1})	12.4	8.4	38.5	33.2	43.3	22.0	13.2	15.9	17.4	23.7	35.1	37.0	35.0	22.1	31.6	37.5	13.6	12.4
α_r (s^{-1})	13.1	21.8	37.7	30.6	32.0	33.4	19.6	4.3	26.4	3.4	67.7	35.2	24.4	22.3	46.9	47.1	11.1	15.1

Patient 3 (position-based)																		
Zone	1	2	3	4	5	6	7	8	9	10	11	12	13	14	15	16	17	RV
σ_0 (kPa)	46.4	0.0	0.0	2.8	11.1	13.3	15.3	106.8	95.2	38.3	32.6	40.8	20.2	35.0	31.2	49.5	158.3	44.1
α_c (s^{-1})	1.8	2.8	15.3	18.6	5.9	100.0	2.8	0.0	0.0	4.2	2.0	4.0	2.9	2.2	1.3	1.2	0.6	4.3
α_r (s^{-1})	100.0	37.6	9.3	4.2	100.0	100.0	0.0	20.8	19.8	5.2	100.0	100.0	2.4	32.8	25.0	100.0	32.1	100.0

Patient 3 (velocity-based)																		
Zone	1	2	3	4	5	6	7	8	9	10	11	12	13	14	15	16	17	RV
σ_0 (kPa)	16.5	8.2	90.3	21.7	23.5	30.5	24.9	7.8	0.0	46.2	44.5	27.1	10.1	61.6	16.4	15.7	193.3	33.9
α_c (s^{-1})	50.1	55.0	0.0	2.9	63.6	35.3	11.2	16.1	85.1	2.8	1.4	25.7	20.8	2.3	2.8	44.5	0.3	25.6
α_r (s^{-1})	94.4	100	18.1	94.9	66.4	43.1	4.0	0.9	0.5	3.9	52.5	26.6	1.9	28.8	92.4	94.8	40.1	28.5

TABLE IV
VOLUNTEER DATA. ESTIMATED CONTRACTION PARAMETERS.

Volunteer 1 (velocity-based)																		
Zone	1	2	3	4	5	6	7	8	9	10	11	12	13	14	15	16	17	RV
σ_0 (kPa)	108.0	110.2	105.2	102.4	96.4	109.6	89.0	117.7	110.1	96.3	97.7	100.3	89.3	73.0	88.5	89.1	90.3	84.8
α_c (s^{-1})	56.2	22.7	28.1	28.1	33.6	26.2	58.2	11.8	13.6	37.4	34.2	32.1	31.9	40.6	28.4	28.3	26.8	28.9
α_r (s^{-1})	27.9	31.0	27.5	28.8	31.7	25.1	41.9	0.0	18.1	24.0	28.6	33.8	39.7	14.3	33.6	38.0	0.5	32.3

Volunteer 2 (velocity-based)																		
Zone	1	2	3	4	5	6	7	8	9	10	11	12	13	14	15	16	17	RV
σ_0 (kPa)	85.7	108.0	108.6	91.2	84.3	99.6	104.4	112.8	136.8	90.3	90.6	65.1	57.8	81.5	77.8	80.6	101.2	81.7
α_c (s^{-1})	62.6	32.1	22.6	29.4	41.4	48.9	43.1	27.2	20.4	26.1	42.0	51.1	69.7	19.7	20.8	45.8	27.9	25.0
α_r (s^{-1})	42.1	42.8	35.9	32.2	36.9	43.3	29.4	3.2	20.9	19.1	40.4	46.5	19.3	8.4	40.1	26.6	5.3	28.8

Volunteer 3 (velocity-based)																		
Zone	1	2	3	4	5	6	7	8	9	10	11	12	13	14	15	16	17	RV
σ_0 (kPa)	108.7	70.9	93.9	110.1	94.6	89.6	107.8	65.1	128.2	95.4	114.6	83.9	95.2	64.6	98.3	83.6	107.4	81.9
α_c (s^{-1})	38.5	46.9	29.1	30.1	32.6	29.7	46.0	33.7	10.0	40.7	25.0	42.2	22.0	39.3	21.3	29.4	20.1	25.9
α_r (s^{-1})	33.5	53.2	36.0	28.3	32.6	35.6	30.2	3.2	2.6	27.0	36.9	43.5	30.3	58.4	29.3	28.4	25.4	33.0

differences between the contraction rate (α_c) and relaxation rate (α_r) are more obvious. As there is no ground truth, it is impossible to justify which one is more accurate. Nevertheless, we can see that for the position-based optimization, the relaxation rate of the LV is very large and reaches the preset upper bound (100 s^{-1}), which is undesirable.

When the number of zones increases, the differences between the position-based and velocity-based optimizations are more obvious. For Patient 2, the spatial variations of the maximum contractions are similar. Nevertheless, the values of zone 8 and 17 of the position-based optimization reach the preset upper bound (200 kPa). Similar observations are more obvious in the relaxation rates, where the position-based optimization has five zones (5, 6, 7, 8, and 9) reaching the preset upper bound (100 s^{-1}), while all parameters of the velocity-based optimization are within the preset bounds.

For Patient 3, the estimated parameters between the position-based and velocity-based optimizations are more different. The small deformation and the large incoordinate contraction of the left and right ventricles make the estimation more difficult. For the position-based optimization, there are 12 zones (1, 2, 3, 5, 6, 7, 8, 9, 11, 12, 16, and RV) with the parameters reaching the bounds. On the other hand, the velocity-based one has only three zones (2, 3, and 9) reaching the bounds. Therefore, although both estimations were less optimal, the velocity-based estimation gives better results.

As the velocity-based estimation is more optimal, it will be the concentration in our following discussions. To show the realism of the personalized mechanics, the simulated blood pressures through ventricular isovolumetric constraints and Windkessel model are compared with the invasively measured blood pressure of the patients (Fig. 9). The LV blood pressure

and its time derivative show large improvement after mechanics personalization, especially for Patient 3. This means that the personalized electromechanical model can partially reflect the subject's actual physiology.

Fig. 10 provides the comparisons among the personalized kinematics, simulations with initial parameters, and personalized simulations. In all cases, the simulations with the personalized parameters are closer to the personalized kinematics. Fig. 10 also shows the active contraction stresses at the end of systole. For Patient 1, the scar region has lower contractility, which is consistent to the pathology. Nevertheless, the septum and apex also have lower contractility even they are not infarcted. The lower estimated contractility at the septum is probably related to the septal flash of the patient, which is due to a difficulty of the septum to properly contract at the right timing, for which our current model cannot simulate. On the other hand, as the apex is located outside the image region, the estimated contractility is hard to justify. In all three cases, the right ventricles have relatively large contractility than the left ventricles, especially for Patient 2 and 3. This adequately reflects the symptom of dilated cardiomyopathy. The inconsistently high contractilities of the apex of Patient 2 was mainly caused by the imposed displacement boundary conditions, and its location outside of the image region.

B. Healthy Volunteers

1) *Experimental Setups:* To show that our framework can also provide results reflecting healthy cardiac conditions, experiments were performed on volunteers' data without known cardiac diseases. Each data set has a cine MRI sequence of 30 frames, with the heart periods of Volunteer 1, 2, and 3 as 0.83, 0.87, and 1.2 s respectively. All data sets have 1.25 mm^2 in-plane resolution and 10 mm inter-slice resolution. Neither endocardial activation maps nor ventricular blood pressures were measured. The electrical propagations were obtained using simulations with normal parameters [17].

Each heart geometry was segmented from the image frame at mid-diastole, and a FEM mesh with synthetic fiber orientations was constructed. AHA-representations were used. Kinematics personalizations were performed to provide the surface positions and velocities for the experiments. The same optimization settings in the previous section were applied.

2) *Results:* Table IV shows that the estimated maximum contractions of the LV and RV are similar. These are consistent with those in the literature [3]. As the initial parameters roughly account for the normal conditions, their differences with the estimated parameters are smaller than those in the diseased cases. For these healthy volunteers, their apparent heart motion can be well simulated with our model, thus among the 162 estimated parameters, only one α_r at zone 8 of Volunteer 1 reaches the lower bound.

Fig. 11 shows that the personalized simulations are closer to the measurements than the initializations in general, especially for Volunteer 1 and 3. Again, as the initial parameters mainly accounts for the normal conditions, the improvements are not as obvious as those in the diseased cases. All these show that our framework can estimate parameters consistent with the health conditions of the subjects.

VII. DISCUSSION

The results in the synthetic experiments show that the use of velocity-based objective function can better identify the contraction parameters of the given model, and have better convergence rates than the position-based optimization because of the properties of the landscape. In reality, as the ground truth is unavailable, it is difficult to verify which objective functions or algorithms provide better results, especially when both personalized simulations are similar to the measurements. We may justify the realism of a model through its ability of prediction, for example, one can simulate the cardiac resynchronization therapy procedure on a personalized model to see if the prediction matches the interventional measurements [1]. Nevertheless, such a validation is very complicated as it requires the personalization and prediction of both electrophysiology, active contraction, and passive mechanical properties. Therefore, in this paper, our main validation is based on the synthetic experiments to assess the best possible performance of the framework in ideal situations.

Although blood pressure measurements are available in the diseased cases, we have not utilized them in the personalization. One reason is that such invasive measurements may not be always available, such as the volunteer's data. Another reason is the difficulty of incorporating the pressure data. If we directly apply the measured blood pressures as natural boundary conditions on the endocardial surfaces, the simulations will be more unstable as the heart geometry may collapse because of the inconsistency between the active contractility and the applied pressures. This will lead to more complicated manual adjustment for each case studied. A more flexible way is to embed the pressures into the objective function, but this is not trivial and further investigation is required.

This framework is similar to other parameter estimation frameworks [9], [11], [10], [12], [14], and therefore suffers from the curse of dimensionality. Although the subplex method has already helped to alleviate the problem by decomposing the high-dimensional space into subspaces, the numbers of iterations required are still very large, and it will be computationally very challenging with more number of zones. To address this problem, one possibility is to study the spatial dependencies among different regions to see if hierarchical approaches can be applied. Furthermore, the interactions between parameters within a zone can also be investigated for the possibility of decomposing the estimation, so that the search space can be reduced.

There are several limitations of this framework. First of all, the passive mechanical properties are assumed to be known and homogeneous, but the myocardium is known to be heterogeneous especially in diseased cases. As the reduction of myocardial deformation can be caused by hardening of material, reduction of contractility, or both [2], [3], [31], the assumption of known material properties can lead to suboptimal parameter estimation. In fact, the framework of passive mechanical parameter estimation is also in progress [32], which can be combined with the framework in this paper when both become mature, though the task will be very challenging. Secondly, some of the calibrations were

performed by manual adjustments, for examples, the time differences between the electrical excitation and the onset of the active contraction. Techniques such as that in [13] can help to alleviate this issue.

VIII. CONCLUSION

We presented a velocity-based cardiac contractility personalization framework using the derivative-free subplex optimization. With derivative-free optimization, analytical and numerical difficulties associated with gradient evaluation can be avoided, and an objective function accounting for the velocity differences between simulations and measurements was proposed to personalize cardiac contractility. Experiments on synthetic data show that the maximum contraction, contraction rate, and relaxation rate can be better identified using the velocity-based optimization than the position-based optimization. Experiments on clinical data show that the proposed framework can identify parameters consistent to the subject-specific physiologies of both patients and healthy volunteers.

REFERENCES

- [1] M. Sermesant, R. Chabiniok, P. Chinchapatnam, T. Mansi, F. Billet, P. Moireau, J.-M. Peyrat, K. C. L. Wong, J. Relan, K. S. Rhode, M. Ginks, P. Lambiase, H. Delingette, M. Sorine, C. A. Rinaldi, D. Chapelle, R. Razavi, and N. Ayache, "Patient-specific electromechanical models of the heart for the prediction of pacing acute effects in CRT: A preliminary clinical validation," *Medical Image Analysis*, vol. 16, no. 1, pp. 201–215, 2012.
- [2] L. Glass, P. Hunter, and A. McCulloch, Eds., *Theory of Heart: Biomechanics, Biophysics, and Nonlinear Dynamics of Cardiac Function*. Springer-Verlag, 1991.
- [3] W. J. Germann and C. L. Stanfield, *Principles of Human Physiology*. Pearson Benjamin Cummings, 2005.
- [4] M. Nash, "Mechanics and material properties of the heart using an anatomically accurate mathematical model," Ph.D. dissertation, The University of Auckland, 1998.
- [5] T. P. Usyk, I. J. LeGrice, and A. D. McCulloch, "Computational model of three-dimensional cardiac electromechanics," *Computing and Visualization in Science*, vol. 4, no. 4, pp. 249–257, 2002.
- [6] M. Sermesant, H. Delingette, and N. Ayache, "An electromechanical model of the heart for image analysis and simulation," *IEEE Transactions on Medical Imaging*, vol. 25, no. 5, pp. 612–625, 2006.
- [7] K. C. L. Wong, L. Wang, H. Zhang, H. Liu, and P. Shi, "Meshfree implementation of individualized active cardiac dynamics," *Computerized Medical Imaging and Graphics*, vol. 34, no. 1, pp. 91–103, 2010.
- [8] Z. Hu, D. Metaxas, and L. Axel, "In vivo strain and stress estimation of the heart left and right ventricles from MRI images," *Medical Image Analysis*, vol. 7, no. 4, pp. 435–444, 2003.
- [9] H. Liu and P. Shi, "Maximum a posteriori strategy for the simultaneous motion and material property estimation of the heart," *IEEE Transactions on Biomedical Engineering*, vol. 56, no. 2, pp. 378–389, 2009.
- [10] R. Chabiniok, P. Moireau, P.-F. Lesault, A. Rahmouni, J.-F. Deux, and D. Chapelle, "Trials on tissue contractility estimation from cardiac cine MRI using a biomechanical heart model," in *International Conference on Functional Imaging and Modeling of the Heart*, ser. LNCS, vol. 6666. Springer, 2011, pp. 304–312.
- [11] V. Y. Wang, H. I. Lam, D. B. Ennis, B. R. Cowan, A. A. Young, and M. P. Nash, "Modelling passive diastolic mechanics with quantitative MRI of cardiac structure and function," *Medical Image Analysis*, vol. 13, no. 5, pp. 773–784, 2009.
- [12] J. Xi, P. Lamata, J. Lee, P. Moireau, D. Chapelle, and N. Smith, "Myocardial transversely isotropic material parameter estimation from in-silico measurements based on reduced-order unscented Kalman filter," *Journal of the Mechanical Behavior of Biomedical Materials*, vol. 4, no. 7, pp. 1090–1102, 2011.
- [13] S. Marchesseau, H. Delingette, M. Sermesant, K. Rhode, S. Duckett, C. Aldo Rinaldi, R. Razavi, and N. Ayache, "Cardiac mechanical parameter calibration based on the unscented transform," in *International Conference on Medical Image Computing and Computer Assisted Intervention*, ser. LNCS, vol. 7511. Springer, 2012, pp. 41–48.
- [14] H. Delingette, F. Billet, K. C. L. Wong, M. Sermesant, K. Rhode, M. Ginks, C. A. Rinaldi, R. Razavi, and N. Ayache, "Personalization of cardiac motion and contractility from images using variational data assimilation," *IEEE Transactions on Biomedical Engineering*, vol. 59, no. 1, pp. 20–24, 2012.
- [15] K. J. Bathe, *Finite Element Procedures*. Prentice Hall, 1996.
- [16] T. Belytschko, Y. Krongauz, D. Organ, M. Fleming, and P. Krysl, "Meshless methods: an overview and recent developments," *Computer Methods in Applied Mechanics and Engineering*, vol. 139, no. 1-4, pp. 3–47, 1996.
- [17] M. Sermesant, P. Moireau, O. Camara, J. Sainte-Marie, R. Andriantsimavona, R. Cimrman, D. L. G. Hill, D. Chapelle, and R. Razavi, "Cardiac function estimation from MRI using a heart model and data assimilation: advances and difficulties," *Medical Image Analysis*, vol. 10, pp. 642–656, 2006.
- [18] K. Rhode, M. Sermesant, D. Brogan, S. Hegde, J. Hipwell, P. Lambiase, E. Rosenthal, C. Bucknall, S. Qureshi, J. Gill, R. Razavi, and D. Hill, "A system for real-time XMR guided cardiovascular intervention," *IEEE Transactions on Medical Imaging*, vol. 24, no. 11, pp. 1428–1440, 2005.
- [19] J. Relan, P. Chinchapatnam, M. Sermesant, K. Rhode, M. Ginks, H. Delingette, C. A. Rinaldi, R. Razavi, and N. Ayache, "Coupled personalization of cardiac electrophysiology models for prediction of ischaemic ventricular tachycardia," *Journal of the Royal Society Interface Focus*, vol. 1, no. 3, pp. 396–407, 2011.
- [20] F. Billet, M. Sermesant, H. Delingette, and N. Ayache, "Cardiac motion recovery and boundary conditions estimation by coupling an electromechanical model and cine-MRI data," in *International Conference on Functional Imaging and Modeling of the Heart*, ser. LNCS, vol. 5528. Springer, 2009, pp. 376–385.
- [21] K. C. L. Wong, F. Billet, T. Mansi, R. Chabiniok, M. Sermesant, H. Delingette, and N. Ayache, "Cardiac motion estimation using a proactive deformable model: evaluation and sensitivity analysis," in *Statistical Atlases and Computational Models of the Heart*, ser. LNCS, vol. 6364. Springer, 2010, pp. 154–163.
- [22] H. Sundar, C. Davatzikos, and G. Biro, "Biomechanically-constrained 4D estimation of myocardial motion," in *International Conference on Medical Image Computing and Computer Assisted Intervention*, ser. LNCS, vol. 5762. Springer, 2009, pp. 257–265.
- [23] P. Moireau, D. Chapelle, and P. Le Tallec, "Joint state and parameter estimation for distributed mechanical systems," *Computer Methods in Applied Mechanics and Engineering*, vol. 197, no. 6-8, pp. 659–677, 2008.
- [24] A. R. Conn, K. Scheinberg, and L. N. Vicente, *Introduction to Derivative-Free Optimization*. Society for Industrial Mathematics, 2009, vol. 8.
- [25] S. S. Rao, *Engineering Optimization: Theory and Practice*. John Wiley & Sons, Inc., 2009.
- [26] M. J. D. Powell, "On trust region methods for unconstrained minimization without derivatives," *Mathematical Programming*, vol. 97, no. 3, pp. 605–623, 2003.
- [27] T. Rowan, "Functional stability analysis of numerical algorithms," Ph.D. dissertation, University of Texas at Austin, 1990.
- [28] J. A. Nelder and R. Mead, "A simplex method for function minimization," *Computer Journal*, vol. 7, no. 4, pp. 308–313, 1965.
- [29] M. D. Cerqueira, N. J. Weissman, V. Dilisizian, A. K. Jacobs, S. Kaul, W. K. Laskey, D. J. Pennell, J. A. Rumberger, T. Ryan, and M. S. Verani, "Standardized myocardial segmentation and nomenclature for tomographic imaging of the heart: a statement for healthcare professionals from the cardiac imaging committee of the council on clinical cardiology of the American Heart Association," *Circulation*, vol. 105, pp. 539–542, 2002.
- [30] M. Sermesant, F. Billet, R. Chabiniok, T. Mansi, P. Chinchapatnam, P. Moireau, J. Peyrat, K. Rhode, M. Ginks, P. Lambiase, S. Arridge, H. Delingette, M. Sorine, C. Aldo Rinaldi, D. Chapelle, R. Razavi, and N. Ayache, "Personalised electromechanical model of the heart for the prediction of the acute effects of cardiac resynchronisation therapy," in *International Conference on Functional Imaging and Modeling of the Heart*, ser. LNCS, vol. 5528. Springer, 2009, pp. 239–248.
- [31] E. Braunwald, D. P. Zipes, and P. Libby, Eds., *Heart Disease: A Textbook of Cardiovascular Medicine*, 6th ed. W.B. Saunders Company, 2001.
- [32] K. C. L. Wong, J. Relan, L. Wang, M. Sermesant, H. Delingette, N. Ayache, and P. Shi, "Strain-based regional nonlinear cardiac material properties estimation from medical images," in *International Conference on Medical Image Computing and Computer Assisted Intervention*, ser. LNCS, vol. 7510. Springer, 2012, pp. 617–624.

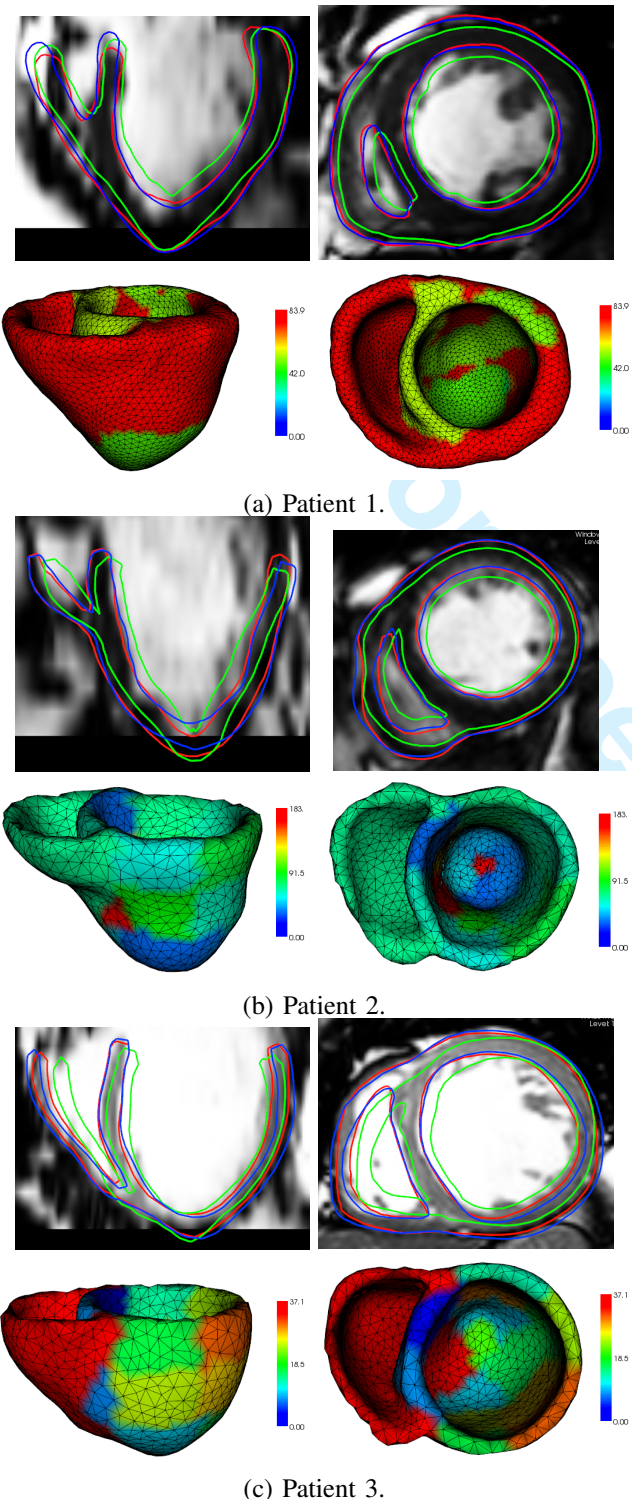


Fig. 10. Patient data. Results at end systole. Top: heart geometries overlapped with images, with red, green, and blue representing personalized kinematics, initializations, and personalized simulations respectively. Bottom: personalized simulations and the corresponding contraction stresses in kPa.

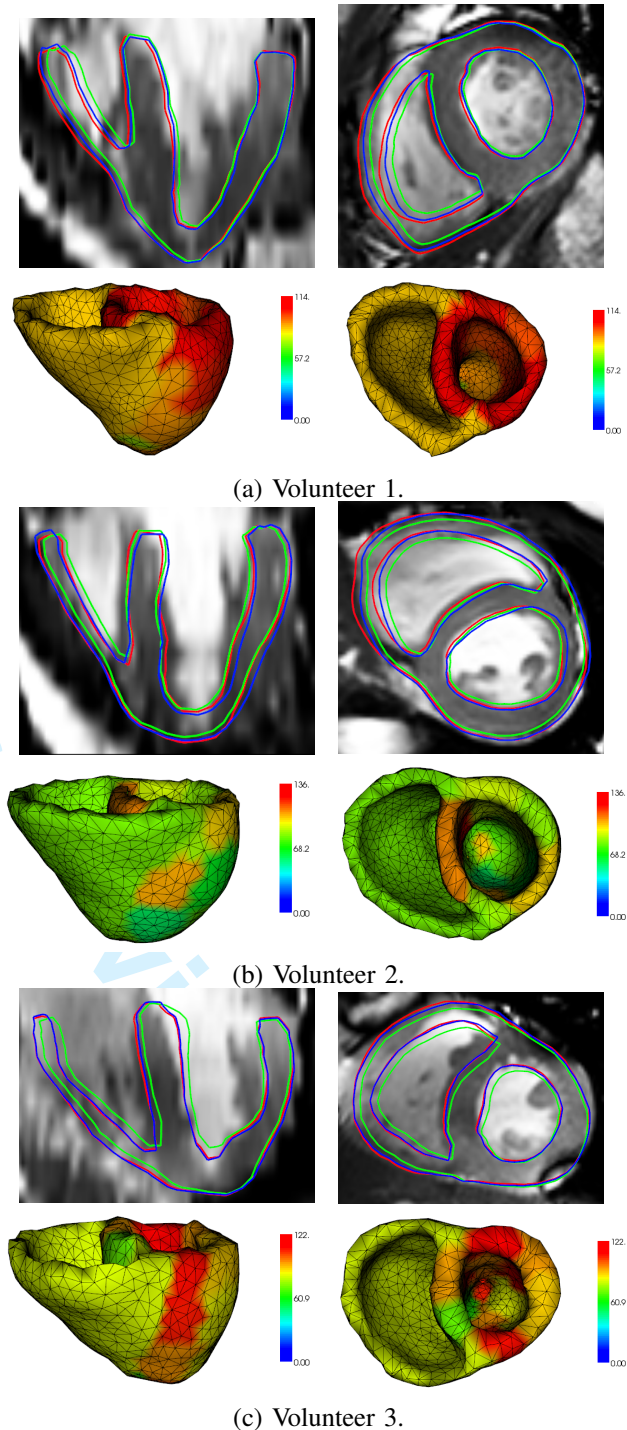


Fig. 11. Volunteer data. Results at end systole. Top: heart geometries overlapped with images, with red, green, and blue representing personalized kinematics, initializations, and personalized simulations respectively. Bottom: personalized simulations and the corresponding contraction stresses in kPa.